OBSERVATIONAL CONSTRAINTS ON NON-LORENTZIAN CONTINUUM EFFECTS IN THE NEAR-INFRARED SOLAR SPECTRUM USING ARM ARESE DATA

A. M VOGELMANN†, V. RAMANATHAN, W. C. CONANT and
W. E. HUNTER

Center for Atmospheric Sciences and Center for Clouds, Chemistry and Climate, Scripps Institution of
Oceanography, University of California, San Diego, La Jolla, CA 92093-0221, U.S.A.

Abstract—Uncertainties exist in the magnitude of the water vapor continuum at solar wavelengths and many models do not include a solar continuum. We assess whether the neglect of the continuum in some models could explain a significant amount of the excess solar absorption found by several recent studies, in which the observed atmospheric solar absorption is significantly greater than that modeled. Towards this goal, we constrain the magnitude of the near-infrared water vapor continuum absorption using observations from the Atmospheric Radiation Measurement (ARM) Enhanced Shortwave Experiment (ARESE). Narrowband irradiances measured by two independent Multifilter Rotating Shadowband Radiometers (MFRSRs) are used to infer the clear-sky transmission by water vapor in the 0.94 μm band. Over 16 000 such observations are compared to non-continuum (i.e., a pure Lorentzian model) and continuum calculations using a correlated-k distribution model, which shows excellent agreement with a line-by-line model and uses coincident measurements of the pressure, temperature and water vapor profiles. Continuum calculations use the CKD super-Lorentzian formulation. The data suggest the need for a far wing continuum in the 0.94 μm band with an absorption that falls between that computed for pure Lorentzian lines and the CKD continuum. A sensitivity analysis presents the effects of uncertainties in parameters affecting the calculations, including those in the line parameters, continuum magnitude and atmospheric state. Upper estimates for the absorption of broadband solar radiation by the continuum, beyond that computed for pure Lorentzian far wings, are only 1 to 2 W m^{-2} for a diurnal (24 h) average, and 4 to 6 W m^{-2} for local noon. Thus, uncertainties in or the neglect of the water vapor continuum at solar wavelengths are not likely explanations for excess absorption of the order of 15 to 30 W m^{-2} (diurnal average). ⓒ 1998 Published by Elsevier Science Ltd. All rights reserved

1. INTRODUCTION

Several recent studies[1-7] conclude that the observed atmospheric solar absorption is systematically underestimated by models (see reviews of earlier work in Refs. 8, 9 and 10). Typically, the observed estimates of absorption in average skies exceed computed estimates by 15 to 30 W m^{-2} on a global and diurnal (24 h) average. However, there is considerable disagreement amongst these studies as to the magnitude of this excess absorption, and whether it is in clear, cloudy or average skies. For example, the suggestion that the excess absorption of the order of 25 to 30 W m^{-2} (diurnal and global average) is in cloudy skies is actively debated.[6,11-14] A number of physical mechanisms have been proposed as contributing to excess absorption (see reviews mentioned earlier), but a complete explanation yet remains uncertain.

Of the studies that find significant excess absorption in clear skies,[2,6,7] Arking[6] estimates this excess absorption to be 25 to 30 W m^{-2} (diurnal and global average) and that it is correlated with water vapor amount and uncorrelated with cloud amount. This implies that model treatments of water vapor absorption may be inadequate, or that models do not account for absorbers that correlate with water vapor. Potential sources of uncertainty in the modeling water

---

†To whom correspondence should be addressed.

vapor absorption include the treatment and magnitude of the near-infrared water vapor continuum.

The existence and treatment of the water vapor continuum have long been a subject of debate within the atmospheric sciences community. The debate has focused primarily on the infrared and millimeter-wave windows, but it also has implications for water vapor absorption at near-infrared wavelengths, where water vapor is the primary absorber of solar radiation. While there is widespread agreement on the density dependence and general agreement on the temperature dependence of the continuum, there is "considerable disagreement as to the magnitude and physical mechanisms responsible for the absorption".[15] (See Ref. 15 for a brief summary of the various mechanisms.) A review by O'Neill et al[16] suggests that the magnitude of the continuum has significant uncertainties, with near-infrared continuum absorption coefficients from various studies differing from one another by an order of magnitude. Such uncertainties are being narrowed as a result of more rigorous theoretical treatments (e.g., Refs. 15 and 17); however, such efforts have focused primarily on the longwave, and there are few direct, high-resolution measurements of the continuum at near-infrared wavelengths needed for validation in this region. Thus, unlike longwave radiative transfer models, shortwave models typically do not yet include a continuum and its omission might cause an underestimation of the water vapor absorption. For example, a continuum was not present in many of the shortwave models that participated in the Intercomparison of Radiation Codes in Climate Models (ICRCCM).[18] Thus, the treatment of the near-infrared water vapor continuum presents a potential uncertainty that warrants exploration.

To help address questions regarding excess absorption, the Atmospheric Radiation Measurement (ARM) program, supported by the United States Department of Energy (DOE), initiated the ARM Enhanced Shortwave Experiment (ARESE) to gather the data needed.[19] Our objective is to use ARESE data, a state-of-the-art model of water vapor absorption, and a continuum model to: (1) constrain the magnitude of continuum absorption at near-infrared wavelengths, and (2) assess whether including the continuum in model calculations can explain a significant amount of the excess absorption. Section 2 describes the observations and water vapor absorption models used. Section 3 contains the analysis of observations and computations, and the paper is concluded in Section 4.

We note that the accuracy of near-infrared band models has been addressed for years in the context of retrieving column water vapor from surface observations. The present study is complementary to that body of work, and particularly to Michalsky et al[20] who retrieved water vapor amounts with the same type of radiometer that will be used here. Surface retrieval methods must make assumptions about the vertical distributions of the water vapor and temperature profiles. We make no assumptions about such profiles and use all available information to specify as precisely as possible the pressure and temperature dependent water vapor line broadening. Thus, we are using observations to evaluate as carefully as possible the quality of the model physics that is available to the retrieval methods; in this particular case, the effect of the water vapor continuum.

2. METHOD

2.1. ARESE data

Phase 1 of ARESE was conducted from 21 September to 1 November 1995 in Lamont, Oklahoma, U.S.A. (latitude 36.61°, longitude −97.49°). Column aerosol optical depth and column water vapor transmission are determined from narrowband irradiances measured by a Multifilter Rotating Shadowband Radiometer (MFRSR).[21] The MFRSR has six channels nominally centered at 0.415, 0.5, 0.61, 0.665, 0.862, and 0.94 μm that have full-width-at-half-maxima of approximately 0.01 μm. The channel irradiance is partitioned into direct and diffuse components through the operation of a narrow blade that rotates in and out of the direct solar beam. In this study, we focus on the direct-beam irradiances in the water vapor channel 6 (0.94 μm) and the nearby window channel 5 (0.862 μm), where channel 6 is centered on a strong water vapor absorption band (see Fig. 1). MFRSR irradiances are recorded every 20 sec and the calibration accuracy is estimated to be within 5% (J. Michalsky, personal
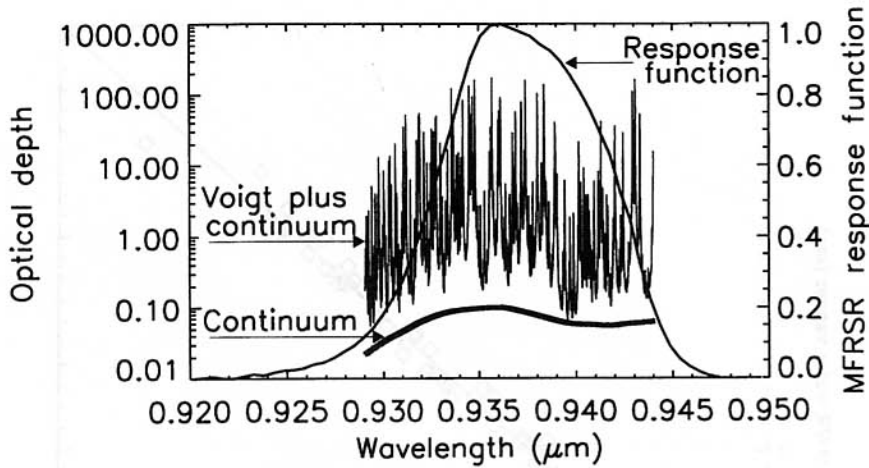
Fig. 1. Water vapor optical depth. Column water vapor optical depths and the continuum contribution are given for the 0.94 μm band of the MFRSR. The curves shown are the Voigt line shape profile computed by the line-by-line model using the CKD_2.2 continuum (Voigt plus continuum curve), the continuum without the Voigt strong line center (continuum curve), and the MFRSR response function that has been normalized so that its peak value is unity. The atmospheric profile is from a sounding from ARESE obtained from a sonde launched 1 October 1995 at 17.41 GMT. The column water vapor amount is 1.34 cm, and the solar zenith angle is 45°.

communication) with a reproducibility of better than 1%. Two MFRSRs are located within 10 m of each other at the ARM site; one is operated as part of the Solar and Infrared Radiation Observing System (SIROS), and the other as part of the Baseline Surface Radiation Network (BSRN). This study will use data primarily from the SIROS MFRSR.

Profiles of pressure, temperature and atmospheric water vapor needed for the modeling were measured by Vaisala balloon sondes that were launched every 3 h. The estimated accuracy of the column water vapor obtained from the sondes is 5%. Column water vapor between sonde launches is retrieved every 20 sec from microwave radiometer (MWR) measurements. The MWR is a Radiometrics Model WVR-1100 that is zenith pointing and measures the atmospheric brightness temperature at 23.8 and 31.4 GHz. Column water vapor is retrieved by inverting the brightness temperatures using a microwave radiative transfer algorithm.[22] The MWR data from the ARM archive has been reprocessed as advised by the instrument mentor to remove the tuning function (J. Liljegren, personal communication). The coincident, independent measures of column water vapor by the sondes and the MWR show excellent agreement for clear-sky days during ARESE, with a mean bias of 1% and root-mean-square (RMS) variance of 5% (Fig. 2). We note that this level of agreement found is markedly better than that typically found between various measurements of column water vapor.

Only cloud-free days from the ARESE period are used. Our cloud-free criteria are: (1) the direct beam irradiance in the visible MFRSR channels must change smoothly with solar zenith angle; (2) the morning and afternoon irradiances must be nearly equal for the same solar zenith angle (i.e., no large atmospheric transmission changes within the day); and (3) a Belfort Laser Ceilometer (a zenith-pointing laser that detects cloud base up to 7800 m) must register no clouds during daylight hours. Additional criteria to detect clouds outside the direct beam are not necessary since we use only direct beam irradiances for this study. Considering these criteria, 11 days from the entire ARESE period are classified as cloud free. Data for each day are used when the solar zenith angle is less than 72.5° (cosine of the solar zenith angle is greater than 0.3), where the cosine response of the MFRSR is well behaved and the air mass scales as the secant of the solar zenith angle (i.e., spherical atmosphere effects are negligible). The sampling frequency of 20 sec provides over 16 000 pairs of irradiance and water vapor measurements with which to conduct this study.
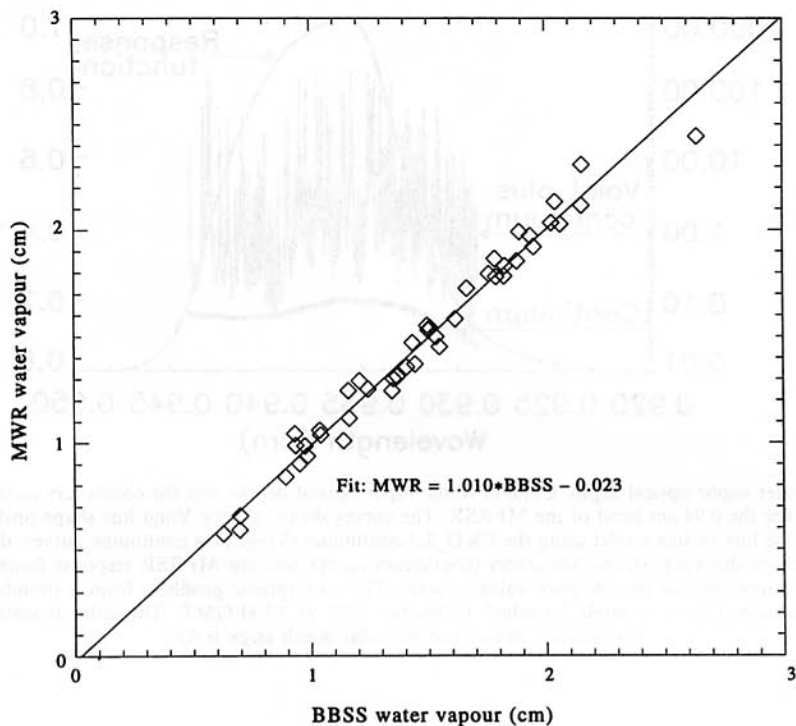
Fig. 2. Microwave radiometer (MWR) comparison to sondes. Column integrated water vapor amounts from the MWR and sondes from the balloon-borne sounding system (BBSS) are compared for clear-sky days during ARESE. The least squares regression plotted gives the average relationship between the BBSS and the MWR column water vapor.

2.2. MFRSR water vapor transmission determination

The MFRSR measures an average flux over a narrow spectral band from which we retrieve the water vapor transmission. The band-average transmission of the direct beam irradiance in the MFRSR water vapor channel 6, T_6, is determined by,

$$T_6 = \frac{I_{6,\text{MFRSR}}}{I_{0,6}} = \frac{\int f_6(\lambda)I_0(\lambda)T(\lambda)\,d\lambda}{\int f_6(\lambda)I_0(\lambda)\,d\lambda} \tag{1}$$

where $I_{6,\text{MFRSR}}$ is the measured channel irradiance, and $I_{0,6}$ is the channel irradiance at the top of the atmosphere. $f_6(\lambda)$ is the filter response function for channel 6, which satisfies the condition $\int_{\lambda_1}^{\lambda_2} f_6(\lambda)\,d\lambda = 1$ where λ_1 and λ_2 delimit the bandpass wavelengths. $I_0(\lambda)$ is the spectral flux at the top of the atmosphere given by $I_0(\lambda) = \varepsilon\mu S_0(\lambda)$, where $S_0(\lambda)$ is the extraterrestrial solar irradiance normally incident on a plane at the mean Earth–Sun distance, ε is the Earth–Sun distance correction factor for the time of the year, and μ is the cosine of the solar zenith angle. $T(\lambda)$ is the direct beam, monochromatic atmospheric transmission given by Beer's Law. $T(\lambda)$ at channel 6 wavelengths is,

$$T(\lambda) = \exp\left(-\frac{\tau_{\text{Ray}}(\lambda) + \tau_{\text{aer}}(\lambda) + \tau_{\text{H2O}}(\lambda)}{\mu}\right) \tag{2}$$

where $\tau_{\text{Ray}}(\lambda)$, and $\tau_{\text{aer}}(\lambda)$, $\tau_{\text{H2O}}(\lambda)$ are, respectively, the Rayleigh, aerosol, and water vapor extinction optical depths. $I_0(\lambda)$, $\tau_{\text{Ray}}(\lambda)$ and $\tau_{\text{aer}}(\lambda)$ are effectively constant across the narrow 0.01 μm band and may be moved outside the integral in Equation (1) and replaced by their band-average values, respectively, $I_{0,6}$, $\tau_{\text{Ray},6}$ and $\tau_{\text{aer},6}$. Equation (1) becomes,

$$T_6 = \exp\left(-\frac{\tau_{Ray,6} + \tau_{aer,6}}{\mu}\right) <T_{H2O}>_{DATA} \tag{3}$$

where

$$<T_{H2O}>_{DATA} \equiv \int f_6(\lambda) \exp\left(-\frac{\tau_{H2O}(\lambda)}{\mu}\right) d\lambda \tag{4}$$

is the band-average transmission due to water vapor in channel 6. For comparison with model calculations, we found it convenient to use minus the natural logarithm of $<T_{H2O}>_{DATA}$,

$$-\ln<T_{H2O}>_{DATA} = -\ln\left(\frac{I_{6,MFRSR}}{I_{0,6}}\right) - \frac{\tau_{Ray,6} + \tau_{aer,6}}{\mu} \tag{5}$$

Note that $-\ln<T_{H2O}>_{DATA}$ is implicitly a function of μ.

$-\ln<T_{H2O}>_{DATA}$ is determined from Equation (5) for each clear-sky MFRSR measurement. The extraterrestrial solar spectrum is obtained at a 0.002 μm resolution.[23,24] The solar zenith angle and Earth–Sun distance correction is computed by the solar ephemeris in Ref. 25 as modified by Ref. 26. The Rayleigh scattering optical depth is computed from sonde data and Ref. 27. $\tau_{aer,6}$ is assumed equal to the aerosol optical depth in channel 5, $\tau_{aer,5}$. This is justified by analyses that find equivalent results for alternative aerosol treatments (see Section 3.2). An advantage to using the measured channel 5 aerosol is that it will implicitly include any effects of undetected thin cirrus and any aerosol size variation with humidity.

The transmission in channel 5 is governed primarily by Rayleigh and aerosol scattering and $\tau_{aer,5}$ is determined from an equation similar to Equation (5),

$$\tau_{aer,5} = -\mu \ln\left(\frac{I_{5,MFRSR}}{I_{0,5}}\right) - \tau_{Ray,5} \tag{6}$$

Prior to determining $\tau_{aer,5}$, channel 5 was calibrated by a method that is essentially equivalent to the empirical Langley method described in Ref. 28. Water vapor absorption in channel 5 is ignored because calculations with a Lorentzian or with a continuum model (described later) show that any weak line or far wing water vapor absorption likely in this region will be dominated by the aerosol optical depth. (This assumption is further supported by the analysis in Section 3.2 which finds the same results when channel 2 (0.5 μm) is used to infer aerosol optical depth.) Table 1 gives the average, maximum and minimum values of column water vapor and $\tau_{aer,5}$ for the 11 clear-sky ARESE days.

The dominant uncertainty in $-\ln<T_{H2O}>_{DATA}$ obtained by this method comes from the instrument calibration uncertainty of 5% in channel 6. This percentage uncertainty in surface irradiance translates to an absolute uncertainty of 0.05 in $-\ln<T_{H2O}>_{DATA}$.

Table 1. Values for the column amounts of water vapor and channel 5 aerosol optical depth for the 11 clear-sky ARESE days. The aerosol optical depth is derived by the method described in the text.

October date	Water vapor column (cm)			Channel 5 aerosol optical depth		
	Average	Minimum	Maximum	Average	Minimum	Maximum
1	1.32	1.21	1.57	0.024	0.017	0.041
4	1.42	1.28	1.62	0.024	0.020	0.031
6	1.17	1.10	1.23	0.029	0.016	0.234
8	1.84	1.57	2.16	0.056	0.051	0.079
11	1.99	1.85	2.16	0.049	0.038	0.060
12	1.64	1.46	1.79	0.048	0.038	0.064
14	0.87	0.79	0.94	0.025	0.018	0.033
15	1.16	0.92	1.40	0.019	0.012	0.027
18	1.73	1.58	1.86	0.057	0.048	0.065
20	0.57	0.47	0.64	0.026	0.016	0.043
28	0.96	0.89	1.02	0.027	0.020	0.070

2.3. Water vapor transmission modeling

2.3.1. Line-by-line calculations. The modeled water vapor transmission is computed by line-by-line and correlated-k distribution algorithms. The algorithms used are modified versions of those provided by W. Ridgway of Applied Research Corporation working at the Goddard Space Flight Center of the National Aeronautic and Space Administration. The line-by-line model computes monochromatic optical depths from line parameters determined from laboratory measurements. The line centers, strengths, and half-widths are obtained for a reference pressure and temperature from the HITRAN '92 database.[29] Calculations use a Voigt line shape profile computed by the method in Ref. 30. The calculations include four of the most common water vapor isotopes and the effects of self and foreign half-width broadening. The strength of line i, S_i, at an arbitrary temperature T is determined by,[31]

$$S_i(T) = S_i(T_0)\left(\frac{T_0}{T}\right)^R \frac{Q_v(T_0)}{Q_v(T)} \frac{1 - \exp(-hcv_i/kT)}{1 - \exp(-hcv_i/kT_0)} \exp\left[\frac{hcE_i}{k}\left(\frac{1}{T_0} - \frac{1}{T}\right)\right] \tag{7}$$

where $S_i(T_0)$ is the line intensity at the reference temperature, R is the rotational partition function temperature coefficient, Q_v is the vibrational partition function, v_i is the wavenumber of the line center, E_i is the energy of the lower state of transition, h is Planck's constant, k is the Boltzmann constant, and c is the speed of light. The foreign broadened half-width at an arbitrary pressure and temperature, $\alpha_i(p,T)$, is scaled from that at a reference pressure and temperature, $\alpha_i(p_0,T_0)$, by,

$$\alpha_i(p, T) = \alpha_i(p_0, T_0)\left(\frac{p}{p_0}\right)\left(\frac{T_0}{T}\right)^n \tag{8}$$

where the temperature dependence coefficient, n, is obtained from the HITRAN database. The self-broadened half-widths are computed by an equation similar to Equation (8) where α_i is replaced by the self-broadened half-width, p by the partial pressure of water vapor, and the temperature scaling is the same as for foreign broadening. Line wing contributions within ± 300 cm^{-1} from a given wavenumber are included in the calculations that treat the far wings as being Lorentzian (hereafter such calculations may be referred to as non-continuum calculations). All line-by-line calculations use a spectral resolution of 0.01 cm^{-1}. Higher spectral resolution is not needed because a ten-fold increase in resolution changes $-\ln < T_{\text{H2O}} >_{\text{MODEL}}$ by only 0.01%.

The line-by-line calculations can incorporate the water vapor continuum by Clough et al[32] where the far line wings are treated as having a super-Lorentzian shape. (Hereafter this continuum will be referred to as the CKD continuum and the term continuum, when used in relationship to the calculations, refers to this model.) A Lorentzian line shape is derived assuming that the molecular collisions are instantaneous, while this super-Lorentzian line shape applies a correction to account for the effects of the collision durations. Specifically, the CKD continuum formulation uses a symmetrized power spectral density function where the quotient of the continuum absorption coefficient and the radiation term is denoted by $\tilde{C}(v)$ and given by,[32]

$$\tilde{C}(v) = \sum_i S_i[F_c(v - v_i)\chi'(v - v_i) + F_c(v + v_i)\chi'(v + v_i)] \tag{9}$$

The line transition data is incorporated by $F_c(v \mp v_i)$, a line shape function derived from the instantaneous impact assumption, and $\chi'(v \mp v_i)$ is a semi-empirical function that corrects for the duration of molecular collisions. (Note that there is a typographical error in Ref. 32, Equation (7) has been corrected by using χ' rather than χ.) The F_c function is defined as,[32]

$$F_c(v \mp v_i) = \begin{cases} \dfrac{1}{\pi}\dfrac{\alpha_i}{25^2 + \alpha_i^2} & |v \mp v_i| \leq 25 \text{ cm}^{-1} \\[2ex] \dfrac{1}{\pi}\dfrac{\alpha_i}{(v \mp v_i)^2 + \alpha_i^2} & |v \mp v_i| \geq 25 \text{ cm}^{-1} \end{cases} \tag{10}$$

where most of the strong line center is excluded. The χ' function is fit to get agreement between calculations and observed spectra in the thermal infrared windows. An example of the continuum line shape defined by F_c and χ' for the foreign continuum is the shaded area in Fig. 3 (note that this continuum formulation is also defined at the line center). The complete CKD super-Lorentzian line shape profile is also plotted, accompanied by a standard Lorentzian profile for comparison. The complete CKD line shape profile becomes super-Lorentzian at about ± 5 cm^{-1} from the line center, and then decays exponentially to become sub-Lorentzian ± 100 cm^{-1} from the line center.

A parameterization of the CKD continuum was obtained from the Line-By-Line Radiative Transfer Model (LBLRTM) described in Ref. 33 (version 2.2 is used, identified here by CKD_2.2). The parameterization provides at a given frequency the sum of the neighboring super-Lorentzian far wings (shaded area in Fig. 3). The net effect of the multiple water vapor lines in the 0.94 μm region is to enhance the optical depth as is shown in Fig. 1. Note that in this region the column continuum optical depth is one to two orders of magnitude less than that for the complete Voigt profile calculations using the continuum.

The continuum parameterization was explicitly developed for LBLRTM and is intrinsically linked to line parameter treatments of that model. Use in our line-by-line model is valid only if the line parameter treatments are comparable, and the continuum is correctly installed. It is properly installed, before adding in the continuum, first by subtracting the pedestal (given by top expression in Equation (10)) from the lines, and second by not including any Lorentzian contribution beyond ± 25 cm^{-1}. The consistency of the line treatments between our model and LBLRTM are demonstrated by the close agreement found in both continuum and non-continuum calculations of $-\ln < T_{H2O} >_{MODEL}$. For realistic atmospheres, $-\ln < T_{H2O} >_{MODEL}$ values agree to within 0.012 (1.5%) for continuum cases and 0.019 (2.7%) for the non-continuum cases. This level of agreement is comparable to that typically found in such line-by-line inter-model comparisons; for example, the two line-by-line models in ICRCCM agree in a quantity similar to $-\ln < T_{H2O} >_{MODEL}$ to within 0.004 and 0.011. We note that differences in our continuum and non-continuum comparisons with LBLRTM decrease slightly to 0.008 (1%) for an isothermal atmosphere, which suggests that part of the difference found for the realistic atmospheres arises from how the atmospheric properties between the models are discretized in the vertical.
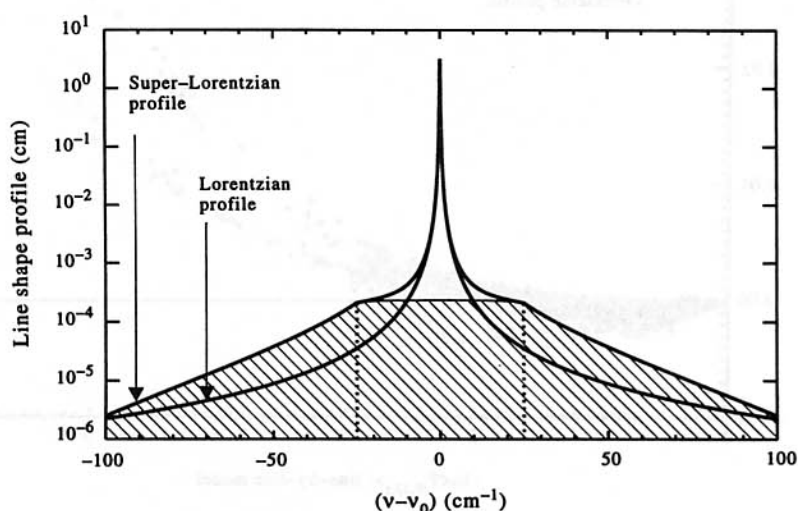

Fig. 3. Line shape profiles. The outermost curve is the line shape profile defined for the complete super-Lorentzian profile with the CKD_2.2 foreign continuum. The shaded region illustrates the line shape for the foreign continuum (only) computed from the bracket in Equation (9) with $i = 1$. A standard Lorentzian line profile (inner, solid line) is given for comparison. The x-axis is the distance from the line center and vertical dotted lines are at ± 25 cm^{-1}.

2.3.2. Correlated-k distributions. The line-by-line model is very precise but is too slow to compute $-\ln < T_{H2O} >_{MODEL}$ for comparison to the 16 000 MFRSR values. A limited number of line-by-line calculations are used to generate correlated-*k* distributions.[34,35] Correlated-*k* distributions are an efficient means of treating gaseous absorption in vertically inhomogeneous, multiple-scattering atmospheres. The key advantage of this method over other band models is that within a band the alignment of spectral (monochromatic) structure between model layers is implicitly maintained or correlated. The assumption of correlation is best for adjacent layers, but it becomes blurred in realistic atmospheres with increasing distance between levels.[36] This approach is exact for a single line and periodic lines of equal intensity,[36] and lines in the strong and weak line limits;[35,36] further, the multiplicative property of transmission of overlapping lines can be incorporated,[35] and the approach is also valid both for absorbing and scattering atmospheres.[35]

The MFRSR channel 6 bandpass is partitioned into 100 sub-bands for which correlated-*k* coefficients are determined from the line-by-line calculations. For comparison with Equation (5), $-\ln < T_{H2O} >_{MODEL}$ is computed by,

$$-\ln\langle T_{H2O}\rangle_{MODEL} = -\ln\left[\frac{\sum_{i=1}^{100} f_{6,i} I_{0,i} T_{H2O,i}\, d\lambda_i}{\sum_{i=1}^{100} f_{6,i} I_{0i}\, d\lambda_i}\right] \qquad (11)$$

where *i* denotes the sub-band interval, $T_{H2O,i}$, is the water vapor transmission computed from the correlated-*k* coefficients for the sub-band, and $f_{6,i}$ and $I_{0,i}$ are, respectively, the response function and solar irradiance incident at the top of the atmosphere for the sub-band. Correlated-*k* computations of surface transmission reproduce the line-by-line calculations from which they are generated to better than 0.6% (Fig. 4). Absorption by molecular species other than water vapor in channel 6 (HF and HCl) is minor and is ignored (those molecules account for only 15 lines of the over 1000 in this region).

Correlated-*k* distributions are generated for the 40 daytime sonde profiles taken during the 11 clear-sky days. Thus, the correlated-*k* coefficients obtain the effects of pressure and temperature
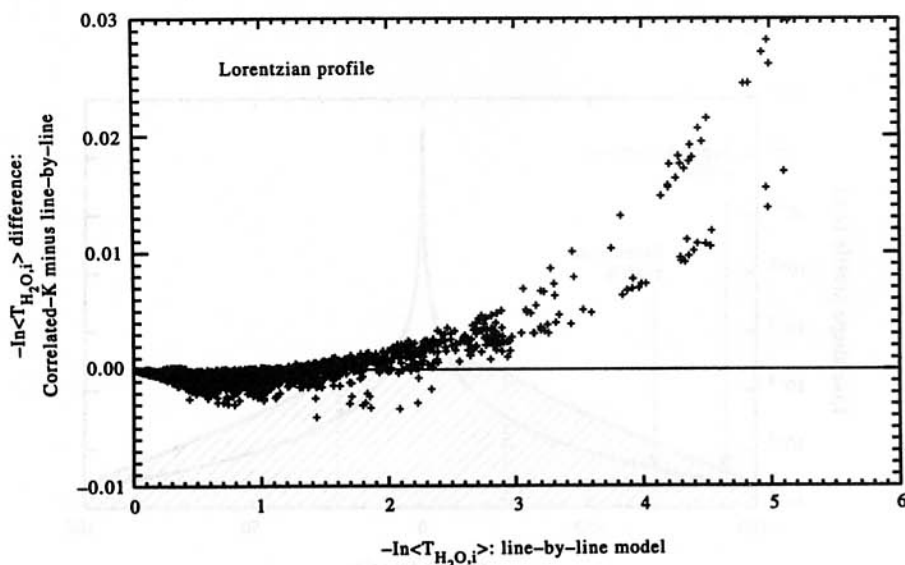

Fig. 4. Correlated-*k* validation. Demonstration that the correlated-*k* coefficients accurately reproduce the line-by-line calculations from which they are derived. $< T_{H2O,i} >$ is the direct beam solar transmission to the surface for the *i*th sub-band; a set of 100 sub-bands spans the wavelength region of the MFRSR response function (each sub-band is approximately 3 cm^{-1} wide). Values are shown for the sub-bands computed from the 40 sonde profiles used in this study. The $-\ln < T_{H2O,i} >$ from the correlated-*k* and line-by-line calculations agree to better than 0.6%.

variations directly from the line-by-line calculations, without resorting to interpolations from pre-computed matrices of pressure and temperatures and any potential uncertainties therein. No attempts are made to interpolate the coefficients between sonde profiles. The water vapor concentrations for each layer are obtained between soundings by scaling the sonde water vapor column to that retrieved by the MWR every 20 sec.

3. RESULTS

3.1. Continuum effects on the observed MFRSR transmission

We use a regression technique to separately identify the bias and the proportionality factor between the observed and computed $-\ln < T_{H2O} >$. A least squares regression is performed for,

$$-\ln\langle T_{H2O}\rangle_{MODEL} = A_0 + A_1\left(-\ln\langle T_{H2O}\rangle_{DATA}\right) \qquad (12)$$

where A_0 and A_1 are determined. We use $-\ln < T_{H2O} >$ rather than $< T_{H2O} >$ in this regression so that any potential errors in transmission that are unrelated to the trending with water vapor loading (e.g., instrumental errors) will be separated in the A_0 term. A_0, the bias or offset, results from a combination of multiple potential sources, including the channel 6 instrument calibration offset and any bias errors in the model physics. For example, the contribution to A_0 of the 0.05 bias uncertainty in $-\ln < T_{H2O} >_{DATA}$ (resulting from the estimated instrument calibration uncertainty) is $0.05A_1$. A_1 is the slope between the computed $-\ln < T_{H2O} >$ and that observed, which shows how well the model can represent the rate at which the atmospheric transmission decreases with an increase in the water vapor path. If theory and observations match exactly, $A_0 = 0$ and $A_1 = 1$. The coefficients A_0 and A_1 are insensitive to subsetting and analysing the data by individual days, or for all days simultaneously but binned by solar zenith angle; the uncertainty in the regression technique is taken to be the greatest RMS variation found which is ± 0.02 in A_0 and in A_1 (details reported in Conant et al[37]).

Many shortwave models assume the line shape to be Lorentzian. Thus, for reference, we first compare the SIROS data to model calculations that treat the far wings as Lorentzian (Fig. 5). The $-\ln < T_{H2O} >_{MODEL}$ are in close agreement with observations. The bias is within the $0.05A_1$ uncertainty from the instrument calibration, and the bias-removed $-\ln < T_{H2O} >_{MODEL}$ underestimates observations by 0.05. The latter differs from unity by two and a half the RMS deviations of the regression technique. The results with the SIROS MFRSR data are validated
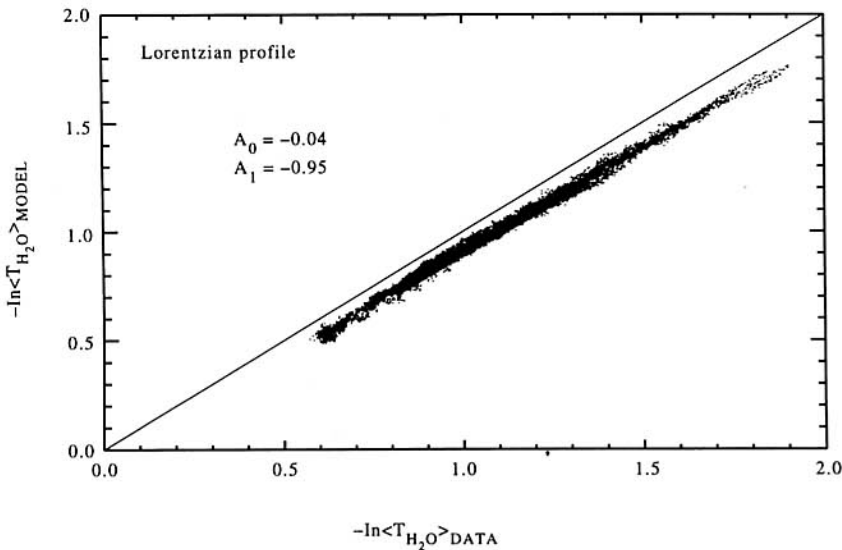

Fig. 5. Lorentzian profile (non-continuum) comparison. Comparison between $-\ln < T_{H2O} >_{DATA}$ and the $-\ln < T_{H2O} >_{MODEL}$ computed with the correlated-k distributions that use a Voigt profile at line center with "Lorentzian" far wings. Coefficients resulting from the regression analysis (Equation (12)) are given in the figure.

Table 2. Sensitivity of the analysis method to water vapor amount. The regressions are performed with the calculations that use a Lorentzian profile. Regressions are performed using all data points (All), and separately for those points with water vapor columns greater than the median (High), and less than the median (Low). Differences between the High and Low regression coefficients from All are negligible (well within the estimated RMS uncertainties of the regression method, ± 0.02 in A_0 and ± 0.02 in A_1).

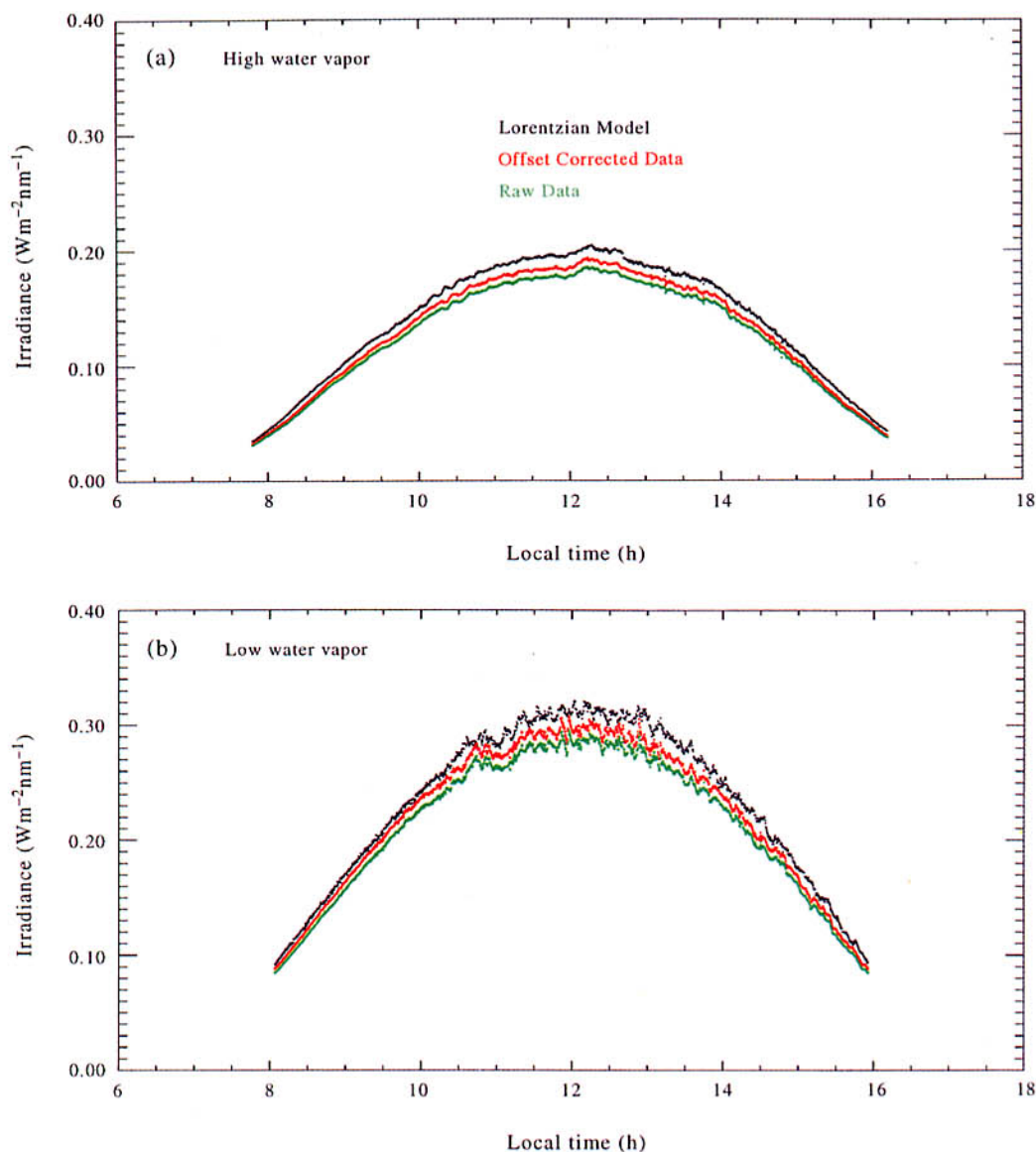| Regression terms	All	High	Low
A_0	-0.04	-0.04	-0.04
A_1	0.95	0.96	0.95

Fig. 6. Observed and modeled direct solar beam irradiances for the 0.94 μm MFRSR channel. Results are given for two ARESE days: (a) a high water vapor content, 1.84 cm on October 8; and (b) a low water vapor content, 0.57 cm on October 20. The model calculations shown assume that the lines are Lorentzian (black curve). Data are shown when the regression offset (A_0) is removed (red, offset corrected data), and without the offset removed (green, raw data). Removing the offset from the data is justified since A_0 is assumed to be due to instrumental uncertainty.

by finding similar results with the BSRN MFRSR, which are an A_0 of -0.06 and an A_1 of 0.93 (see Conant et al[37]).

We test the sensitivity of these results to water vapor amount by computing the regressions separately for high and low water vapor amounts. "High" is defined as the subset of points where the column water vapor amounts are greater than the median, and "Low" is the subset less than the median. The regressions show no significant differences from the complete data set (Table 2).

We plot these observed and modeled direct beam irradiances for the 0.94 μm MFRSR channel for a high and low water vapor day, respectively October 8 and 20 (Fig. 6). An interesting thing to note is that the highly varying temporal features of the data are reproduced by the model calculations with excellent detail. The separation between the calculations (black curve) and the raw observations (green, raw data curve) is largely due to the offset, A_0, which is considered to be explained by the uncertainty in the instrument calibration. With the offset removed from the data (red, data corrected offset curve), the observations and calculations agree on average to within 6%, as would be expected given the similarity shown in Fig. 5. A 6% agreement in the transmission corresponds to a 4% agreement in absorption.

We explore the water vapor transmission further by using super-Lorentzian profile with the CKD continuum in the model calculations (Fig. 7). The bias (A_0) exceeds the uncertainty in instrument calibration by a factor of two, and A_1 increases to 1.10, which differs from unity by more than four times the ± 0.02 RMS uncertainty estimated for the regression technique. The dramatic change effected by the addition of such a small continuum component (see Fig. 1) illustrates the great sensitivity of this regression technique. Thus, the non-continuum calculations are closer to matching the data than the continuum calculations.

The cause for the differences between the Lorentzian and super-Lorentzian regressions (a net change of 0.15 in A_1) is given in Fig. 8 which illustrates the far wing absorption by Lorentzian and CKD super-Lorentzian models in the 0.94 μm region. (Note that the top of the strong line centers are not included in the calculations plotted.) Both models show a rapid decrease in absorption coefficient with wavelength away from the center of the 0.94 μm band, and the average absorption coefficients weighted by the MFRSR response function are 0.010 and 0.056 cm^{-1} for the Lorentzian and super-Lorentzian far wings, respectively. Thus, the super-Lorentzian wing absorption is more than a five-fold enhancement over that for the Lorentzian model.
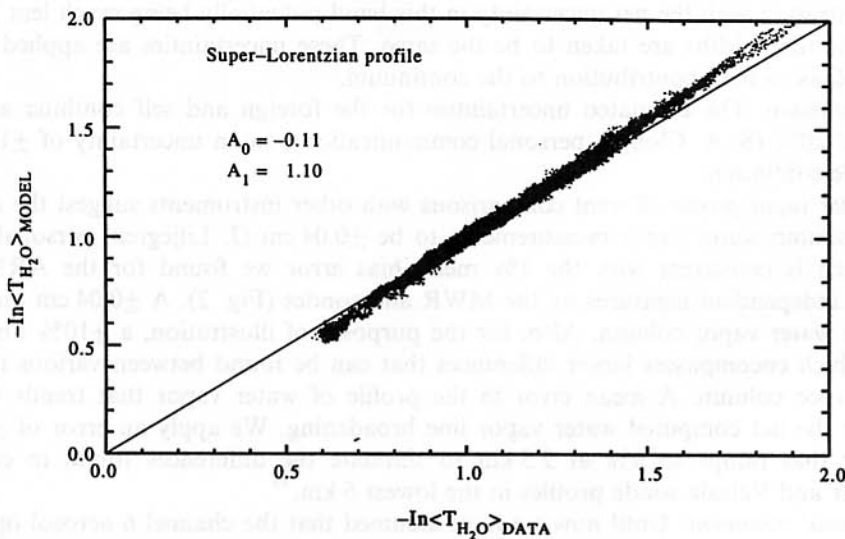

Fig. 7. Super-Lorentzian profile (continuum) comparison. Comparison between $-\ln < T_{H2O} >_{DATA}$ and the $-\ln < T_{H2O} >_{MODEL}$ computed with the correlated-k distributions that use a Voigt profile at line center with the CKD_2.2 continuum treatment. Coefficients resulting from the regression analysis (Equation (12)) are given in the figure.
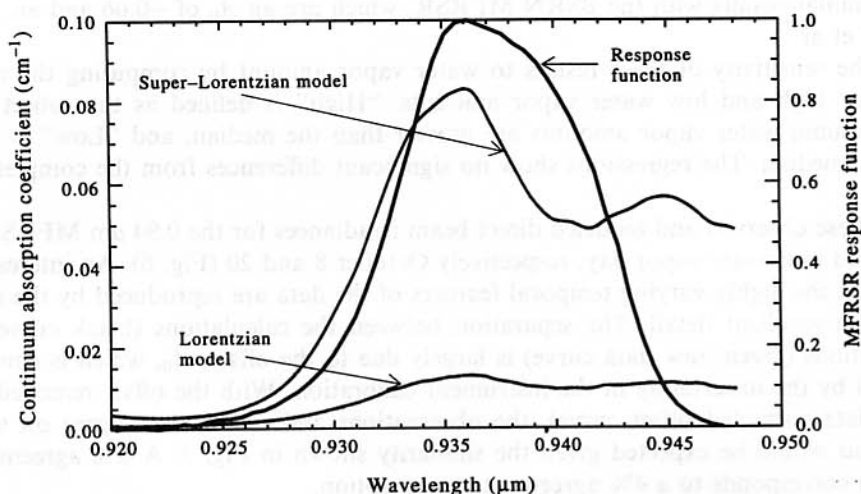
Fig. 8. Continuum absorption coefficients in the vicinity of the MFRSR 0.94 μm channel. The far wing absorption coefficients are given for the CKD_2.2 continuum ("super-Lorentzian Model" curve) and for a pure Lorentzian profile ("Lorentzian Model" curve) where, in both cases, the top of the strong line center is excluded from the complete line shape profile (e.g., the "Lorentzian Model" curve is F_c in Equation (10)). The curves are computed from data inputs for the ARESE period. The response function of the MFRSR channel 6 is superimposed and is normalized so that its maximum value is unity.

3.2. Sensitivity studies

The transmission in a single, narrow water vapor band is potentially sensitive to factors other than the far wing treatment. Thus, the continuum regression results are put into context relative to other uncertainties in the modeling or analysis method by the following sensitivity studies. Of particular interest are uncertainties which can have a large effect and move the calculations towards better agreement with the data. (For reference only, perfect agreement with the data would involve a change of about $+0.11$ in A_0 and about -0.10 in A_1.)

3.2.1. Water vapor lines. Uncertainties of the line strengths in the 0.94 μm region range between 6 and 50%[38] with an average of 20%, but the effective uncertainty resulting from the ensemble RMS errors of the multiple lines is not certain. So uncertainties of ± 10 and $\pm 20\%$ are used for illustration with the net uncertainty in this band potentially being much less. The uncertainties in the half widths are taken to be the same. These uncertainties are applied to the line center as well as to their contribution to the continuum.

3.2.2. Continuum. The estimated uncertainties for the foreign and self continua are, respectively, 15 and 20% (S. A. Clough, personal communication), so an uncertainty of $\pm 15\%$ is used for the whole continuum.

3.2.3. Water vapor profile. Recent comparisons with other instruments suggest the accuracy of the MWR column water vapor measurements to be ± 0.04 cm (J. Liljegren, personal communication), which is consistent with the 1% mean bias error we found for the ARESE period between the independent measures by the MWR and sondes (Fig. 2). A ± 0.04 cm uncertainty is used for the water vapor column. Also, for the purposes of illustration, a $\pm 10\%$ uncertainty is presented which encompasses larger differences that can be found between various measures of the water vapor column. A mean error in the profile of water vapor that trends with height would affect the net computed water vapor line broadening. We apply an error of $\pm 5\%$ at the lowest layer that ramps to 0% at 2.5 km to simulate the differences found in comparisons between lidar and Vaisala sonde profiles in the lowest 6 km.[39]

3.2.4. Aerosol treatment. Until now we have assumed that the channel 6 aerosol optical depth is equal to that in channel 5. We relax that assumption by including an extra term in the regression equation (Equation (12)) of the form $A_2 \tau_n / \mu$, where τ_n is the optical depth for channel n and A_2 is the proportionality constant determined by the regression. We let n be 2 and 5 where the ozone effects are removed from channel 2 (0.5 μm) using the ozone sonde data. Any

significant differences between these regressions might imply, among other things, that significant far wing water vapor absorption is being detected in channel 5.

3.2.5. Extraterrestrial solar spectrum. A constant offset in the solar spectrum could effect A_0, and a difference that depends on wavelength could effect A_0 and A_1. Thus, we repeat our analysis using a different solar spectrum, namely the modeled spectrum by Kurucz[40] (at 1 cm^{-1} resolution) which is used in MODTRAN.[41] In the 0.94 μm region, the Kurucz spectrum is 5.7% greater than the standard spectrum used.

3.2.6. Instrument characteristics. The 5% absolute instrument calibration uncertainty has been addressed by allowing an A_0 as great as ± 0.05. The spectral instrument response function is known to within ± 2 nm at the time of calibration, but the potential of a drift in the water vapor channel must be discussed. (Absolute calibration of other channels, i.e., 2 and 5, was achieved with the Langley-like regression mentioned in Section 2.2, which also corrects for minor drifts.) The BSRN MFRSR calibrations for the water vapor channel before and after the ARESE period agree to within this uncertainty (J. Michalsky, personal communication). A post-ARESE calibration was not performed on the SIROS MFRSR, but a significant drift in the water vapor channel is unlikely given the agreement found between the BSRN and SIROS regressions shown by Conant et al.[37] Thus, the uncertainty used for the response function is ± 2 nm.

The results of the sensitivity analyses are given in Table 3. The regressions using the aerosol optical depths in channels 2 and 5 and the standard case are the same (to within the ± 0.02 RMS uncertainty in the regression method). This indicates that using the channel 5 aerosol optical depth for channel 6 is a good assumption, and that far wing water vapor absorption is not significantly contaminating the standard regression. Changes of the order of $\pm 5\%$ or more in A_1 can be affected only by a $\geq \pm 10\%$ uniform bias error in all of the line intensities or half widths, or in the column water vapor amount. However, no uncertainties significantly decrease the absolute magnitude of A_0 of the order of the $+0.06$ needed to bring it within the estimated uncertainty in the instrument calibration. Thus, such perturbations could explain the data only if, for example, the uncertainty in the instrument offset is doubled, or the top-of-atmosphere solar constant is decreased by 6%.

3.3. Continuum effects on broadband solar absorption

Shortwave models typically neglect the continuum at near-infrared wavelengths and we assess the broadband impact of this assumption. In particular, we determine whether this could affect

Table 3. Regression sensitivity studies. Changes in A_0 and A_1 are provided for uncertainties in the continuum model calculations and analysis method. See text for a description of the uncertainties. A slash separates the results for, respectively, a plus/minus change in the test quantity; only one number is given if the plus/minus results are the same. Perturbations move the regression closer to agreement with the data if they decrease the absolute magnitude of A_0 or decrease A_1. The RMS uncertainty in the regression method is ± 0.02. For reference only, perfect agreement with the data would involve a change of about $+0.11$ in A_0 and about -0.10 in A_1.

Sensitivity test	A_0 change	A_1 change
Kurucz solar spectrum	-0.06	0
Shift MFRSR response function ± 2 nm	$+0.02/-0.01$	-0.03
Regress with aerosol term $A_2\tau_n/\mu$		
Channel 5 aerosol	-0.01	$+0.02$
Channel 2 aerosol	0	-0.02
Water vapor profile		
Water vapor column		
± 0.04 cm	∓ 0.02	0
$\pm 10\%$	$0/+0.01$	$+0.06/-0.07$
Height dependent bias ($\pm 5\%$ at surface, 0% at 2.5 km)	0	0
Line strengths		
$\pm 10\%$	$0/+0.01$	$+0.06/-0.07$
$\pm 20\%$	∓ 0.01	$+0.12/-0.13$
Half widths		
$\pm 10\%$	$0/+0.01$	$+0.04/-0.06$
$\pm 20\%$	∓ 0.02	$+0.11/-0.12$
Continuum		
$\pm 15\%$	∓ 0.01	$+0.02/-0.03$

the absorption by a significant amount relative to the 15 to 30 W m^{-2} (diurnal average) found for excess absorption. We do so by computing the downward solar irradiances at the surface (from 0.5 to 3.5 μm) with a continuum model and with a Lorentzian far wing model; the difference between these calculations is the additional solar absorption effected by the continuum. Four clear-sky profiles are chosen to represent a range of column water vapor amounts found in our climate. Three are from the noontime ARESE profiles, and the fourth is an average tropical profile obtained from the tropical warm pool during the Central Equatorial Pacific Experiment (CEPEX).[42] Diurnal averages of downward surface solar irradiances are computed by a discrete-ordinates-method algorithm[43] using four streams. A standard day is defined as having a solar declination angle of 18.95°, which produces a daylight-average solar zenith angle of 53° at the Oklahoma site and Equator. Only water vapor absorption and Rayleigh scattering are included in this calculation. This calculation will provide an extreme upper estimate for the additional continuum absorption because the standard model with the continuum overestimates the trend with data (Fig. 7), and the exclusion of other gases that absorb in this spectral region (O_3, CO_2, O_2) removes the possibility of their strong line absorption features masking the continuum absorption.

The column water vapor amounts for the profiles are given in Table 4 with the continuum absorption at noontime, and for a diurnal (24 h) average. Upper estimates of the additional continuum absorption are 1 to 2 W m^{-2} for a diurnal average and 4 to 6 W m^{-2} for noontime (Table 4), which are small compared to the estimates for excess absorption that are 15 to 30 W m^{-2} (diurnally averaged). Thus, inclusion of continuum in broadband calculations is an unlikely explanation for excess absorption.

As a final exercise, we assess the potential role of the continuum in excess absorption by determining the increase required in the CKD continuum to explain a significant amount of clear sky excess absorption, and assess whether such an increase is generally consistent with the estimated uncertainties in the continuum or with the data in the 0.94 μm region. We enhance the continuum to increase broadband solar absorption (0.5 to 3.5 μm) above that computed by the Lorentzian profile by approximately 9 W m^{-2} for a diurnal average. We find that this requires a six-fold enhancement in the continuum, which far exceeds its established theoretical uncertainty. Further, when the MFRSR narrowband regression for $-\ln <T_{H2O}>_{MODEL}$ is recomputed with a six-fold continuum increase, it yields extreme differences with the data (Fig. 9). This exercise illustrates that such an increase is clearly not a reasonable possibility and thus could not be a likely explanation for excess absorption of that magnitude.

4. CONCLUSIONS

The trend of $-\ln <T_{H2O}>_{MODEL}$ (in the 0.94 μm band) with water vapor path is underestimated by 5% for calculations assuming pure Lorentzian lines and is overestimated by 10% for

Table 4. Additional continuum broadband solar absorption. Downward total solar irradiances at the surface are computed for the spectral region from 0.5 to 3.5 μm with a continuum model, and with a Lorentzian model; the difference between these calculations is the additional broadband absorption effected by the continuum which is tabulated. Lorentzian wings are truncated ±300 cm^{-1} from line center, and the continuum calculations use the CKD_2.2 continuum. Differences are computed for a standard day (defined in text) and results are presented for a diurnal (24 h) average, and for noontime. The diurnally averaged top-of-atmosphere solar flux is 360 W m^{-2}. Water vapor columns are obtained from clear-sky ARESE and CEPEX balloon sondes. ARESE values are the minimum, median and maximum for noontime launches, and the CEPEX value is an average of several clear-sky days.

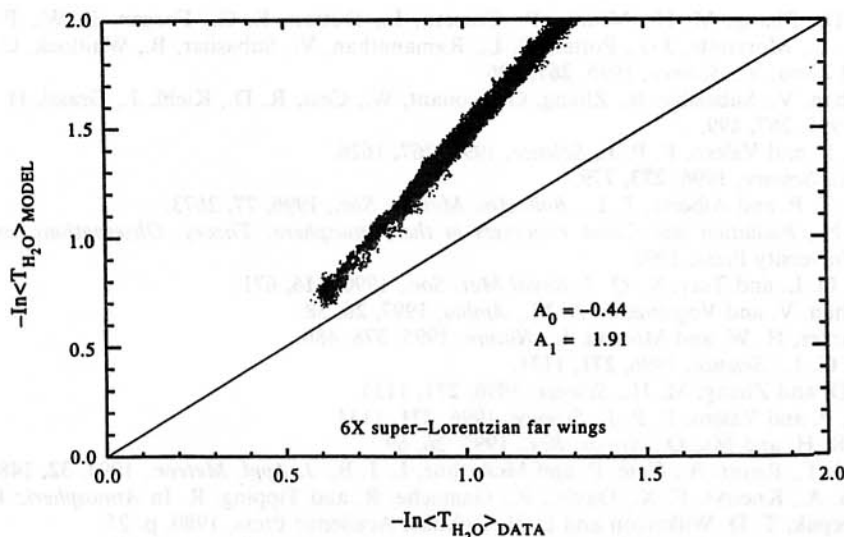| Profile	Water vapor column (cm)	Additional continuum absorption (W m^{-2})	
		24 h average	Noon
ARESE			
Minimum	0.69	1.5	3.9
Median	1.34	1.7	4.4
Maximum	2.04	1.9	4.8
CEPEX	3.94	2.2	5.9

Fig. 9. Comparison for six times the super-Lorentzian far wing continuum. Comparison between $-\ln < T_{H2O} >_{DATA}$ and the $-\ln < T_{H2O} >_{MODEL}$ computed with the correlated-k distributions that use a Voigt profile at line center and six times the CKD_2.2 super-Lorentzian far wing continuum. The factor of six is the amount needed to enhance broadband solar atmospheric absorption by 9 W m^{-2} (diurnal average). Coefficients resulting from the regression analysis (Equation (12)) are given in the figure.

calculations with the CKD continuum (version 2.2). Thus, the data suggest a far wing continuum absorption in this region that is between that computed by pure Lorentzian wings and the CKD continuum. A sensitivity analysis indicates that changes of the order of $\pm 5\%$ or more in this trend can be affected only by a $\geq \pm 10\%$ uniform bias error in all of the line intensities or half widths, or in the column water vapor amount.

The water vapor lines in the 0.94 μm band are a characteristic mix of vibration–rotation lines, so our findings for this band might also apply to other near-infrared wavelengths. However, further studies will be required to constrain the magnitude of a water vapor continuum at other near-infrared wavelengths. The constraints on the continuum within this band or other wavelengths could be further narrowed by a similar analysis with higher resolution radiance data.

Upper estimates for the absorption of broadband solar radiation by the continuum beyond that computed for pure Lorentzian far wings are only 1 to 2 W m^{-2} for a diurnal average and 4 to 6 W m^{-2} for local noon. Thus, uncertainties that exist in the magnitude of the water vapor continuum at solar wavelengths are not a likely explanation for excess absorption of 15 to 30 W m^{-2} (global and diurnally averaged). Enhancements in the modeled continuum absorption are unlikely, as they would further increase the model–observation differences found in the 0.94 μm band. For example, enhancing the continuum absorption to explain 9 W m^{-2} (diurnal average) requires increasing its value by a factor of six, which is many times greater than its estimated theoretical uncertainty and causes extreme disagreements between the model calculations and the observations in the 0.94 μm band.

REFERENCES

1. Ohmura, A. and Gilgen, H., *Am. Geophys. Union Geophys. Monogr.*, 1993, **75**, 93.
2. Wild, M., Ohmura, A., Gilgen, H. and Roeckner, E., *J. Climate*, 1995, **8**, 1309.

3. Cess, R. D., Zhang, M. H., Minnis, P., Corsetti, L., Dutton, E. G., Forgan, B. W., P Garber, D., Gates, W. L., Morcrette, J.-J., Potter, G. L., Ramanathan, V., Subasilar, B., Whitlock, C. H., Young, D. F. and Zhou, Y., *Science*, 1995, **267**, 496.

4. Ramanathan, V., Subasilar, B., Zhang, G., Conant, W., Cess, R. D., Kiehl, J., Grassl, H. and Shi, L., *Science*, 1995, **267**, 499.

5. Pilewskie, P. and Valero, F. P. J., *Science*, 1995, **267**, 1626.

6. Arking, A., *Science*, 1996, **273**, 779.

7. Charlock, T. P. and Alberta, T. L., *Bull. Am. Meteor. Soc.*, 1996, **77**, 2673.

8. Liou, K.-N., *Radiation and Cloud Processes in the Atmosphere: Theory, Observations, and Modeling.* Oxford University Press, 1992.

9. Stephens, G. L. and Tsay, S., *Q. J. Royal Met. Soc.*, 1990, **116**, 671.

10. Ramanathan, V. and Vogelmann, A. M., *Ambio*, 1997, **26**, 38.

11. Li, Z., Barker, H. W. and Moreau, L., *Nature*, 1995, **376**, 486.

12. Stephens, G. L., *Science*, 1996, **271**, 1131.

13. Cess, R. D. and Zhang, M. H., *Science*, 1996, **271**, 1133.

14. Pilewskie, P. and Valero, F. P. J., *Science*, 1996, **271**, 1134.

15. Tipping, R. H. and Ma, Q., *Atmos. Res.*, 1995, **36**, 69.

16. O'Neill, N. T., Royer, A., Coté, P. and McArthur, L. J. B., *J. Appl. Meteor.*, 1993, **32**, 1484.

17. Clough, S. A., Kneizys, F. X., Davies, R., Gamache, R. and Tipping, R. In *Atmospheric Water Vapor*, ed. A. Deepak, T. D. Wilkerson and L. H. Ruhnke. Academic Press, 1980, p. 25.

18. Fouquart, Y., Bonnel, B. and Ramaswamy, V., *J. Geophys. Res.*, 1991, **96**, 8955.

19. Valero, F. P. J., Schwartz, S. E., Cess, R. D., Ramanathan, V., Minnis, P., Ackerman, T. P. and Tooman, T. P., ARESE (ARM Enhanced Shortwave Experiment) Science Plan. Available from the Department of Energy, 1995.

20. Michalsky, J. J., Liljegren, J. C. and Harrison, L. C., *J. Geophys. Res.*, 1995, **100**, 25995.

21. Harrison, L. C., Michalsky, J. J. and Berndt, J., *Appl. Opt.*, 1994, **33**, 5118.

22. Liljegren, J. C. In *Preprints of the Fifth Symposium on Global Change Studies.* American Meteorological Society, Boston, MA, 1994, p. 262.

23. Labs, D. and Neckel, H., *Z. Astrophys.*, 1968, **69**, 1.

24. Smith, E. V. P. and Gottlieb, D. M., *Space Sci. Rev.*, 1974, **16**, 771.

25. Michalsky, J. J., *Solar Energy*, 1988, **40**, 227.

26. Spencer, J. W., *Solar Energy*, 1989, **42**, 353.

27. Bucholtz, A., *Appl. Opt.*, 1995, **34**, 2765.

28. Harrison, L. C. and Michalsky, J. J., *Appl. Opt.*, 1994, **33**, 5126.

29. Rothman, L. S., Gamache, R. R., Tipping, R. H., Rinsland, C. P., Smith, M. A. H., Benner, D. C., Devi, V. M., Flaud, J.-M., Camy-Peyret, C., Perrin, A., Goldman, A., Massie, S. T., Brown, L. R. and Toth, R. A., *JQSRT*, 1992, **48**, 469.

30. Hui, A. K., Armstrong, B. H. and Wray, A. A., *JQSRT*, 1978, **19**, 509.

31. McClatchey, R. A., Benedict, W. S., Clough, S. A., Burch, D. E., Calfee, R. F., Fox, K., Rothman, L. S. and Garing, J. S., *Environ. Res.*, Paper 434, Air Force Cambridge Res. Lab., Bedford, MA, 1973.

32. Clough, S. A., Kneizys, F. X. and Davies, R. W., *Atmos. Res.*, 1989, **23**, 229.

33. Clough, S. A. and Iacono, M. J., *J. Geophys. Res.*, 1995, **100**, 16519.

34. Lacis, A. A. and Oinas, V., *J. Geophys. Res.*, 1991, **96**, 9027.

35. Goody, R., West, M., Chen, L. and Crisp, D., *JQSRT*, 1989, **42**, 539.

36. Fu, Q. and Liou, K.-N., *J. Atmos. Sci.*, 1992, **49**, 2139.

37. Conant, W. C., Vogelmann, A. M. and Ramanathan, V., submitted to *Tellus*, 1997.

38. Chevillard, J.-P., Mandin, J.-Y., Flaud, J.-M. and Camy-Peyret, C., *Can. J. Phys.*, 1989, **67**, 1065.

39. Ferrare, R. A., Melfi, S. H., Whiteman, D. N., Evans, K. D., Schmidlin, F. J. and O'C Starr, D., *J. Atmos. Ocean. Tech.*, 1995, **12**, 1177.

40. Kurucz, R. L. In *Proceedings of the 17th Review Conference on Atmospheric Transmission Models*, Geophysics Directorate/Phillips Laboratory, Hanscom Air Force Base, MA, 1994.

41. Abreu, L. W. and Anderson, G. P. ed., *The MODTRAN 2/3 Report and LOWTRAN7 Model*, Geophysics Directorate/Phillips Laboratory, Hanscom Air Force Base, MA, 1996.

42. Williams, S. F., *Central Equatorial Pacific Experiment (CEPEX) Daily Operations Summary*, The University Corporation for Atmospheric Research Office of Field Support, Boulder, CO, 1993.

43. Stamnes, K., Tsay, S.-C., Wiscombe, W. and Jayaweera, K., *Appl. Opt.*, 1988, **27**, 2502.